

Dynamical Structure Factor from Weak Measurements

E. Altuntas,^{1,2} R. G. Lena,³ S. Flannigan,³ A. J. Daley,^{3,4} and I. B. Spielman²

¹Center for Quantum Research and Technology, Homer L. Dodge Department of Physics and Astronomy, The University of Oklahoma, Norman, OK 73019, USA

²Joint Quantum Institute, National Institute of Standards and Technology, and University of Maryland, Gaithersburg, Maryland, 20899, USA

³Department of Physics and SUPA, University of Strathclyde, G4 0NG Glasgow, UK

⁴Department of Physics, University of Oxford, Clarendon Laboratory, OX1 3PU Oxford, UK
(Dated: September 12, 2024)

Much of our knowledge of quantum systems is encapsulated in the expectation value of Hermitian operators, experimentally obtained by averaging projective measurements. However, dynamical properties are often described by products of operators evaluated at different times; such observables cannot be measured by individual projective measurements, which occur at a single time. For example, the dynamical structure factor describes the propagation of density excitations, such as phonons, and is derived from the spatial density operator evaluated at different times. Conventionally, this is measured by first exciting the system at a specific wavevector and frequency, then measuring the response. Here, we describe an alternative approach using a pair of time-separated weak measurements, and analytically show that their cross-correlation function directly recovers the dynamical structure factor. We provide numerical confirmation of this technique with a matrix product states simulation of the one-dimensional Bose-Hubbard model, weakly measured by phase contrast imaging. We explore the limits of the method and demonstrate its applicability to real experiments with limited imaging resolution.

The properties of many body quantum systems are often encoded in response functions that quantify the reaction of the system to weak external perturbations. The dynamical structure factor (DSF) $S(q, \omega)$, describing a system's response to density perturbations with wavenumber q and frequency ω , derives from the expectation value $\langle \hat{n}(0, 0) \hat{n}(x, t) \rangle$ of the spatial density operator $\hat{n}(x, t)$ at different times and positions [1]. As their name suggests, such quantities are experimentally obtained by observing the system's response to a suitable perturbation: for example neutron scattering gives access to $S(q, \omega)$ in materials [2]. Analogously for ultracold atoms, $S(q, \omega)$ can be obtained by Bragg scattering far-detuned laser light off atomic ensembles [3–6]; the spectral function, a related response function correlating fields rather than densities, can be measured using related techniques [7–9]. By contrast, we focus on measuring density-density correlations $\langle \hat{n}(0, 0) \hat{n}(x, t) \rangle$, and thereby $S(q, \omega)$, by weak quantum measurements alone. This connects to previous work [10], that showed the static structure factor $S(q)$ can be obtained from the same-time density-density correlation function $\langle \hat{n}(0) \hat{n}(x) \rangle$ computed from simple projective measurements of density. Because projective measurements collapse the wavefunction at a well-defined time, they prevent access to the two-time correlations we require.

Generalized quantum measurements, however, allow for weak measurements that minimally disturb the system, but in exchange provide only limited information. These have long been associated with continuous monitoring of both open and closed quantum systems [11, 12], and are essential for closed loop quantum control [13]. Here, we make use of weak measurements in a many-body

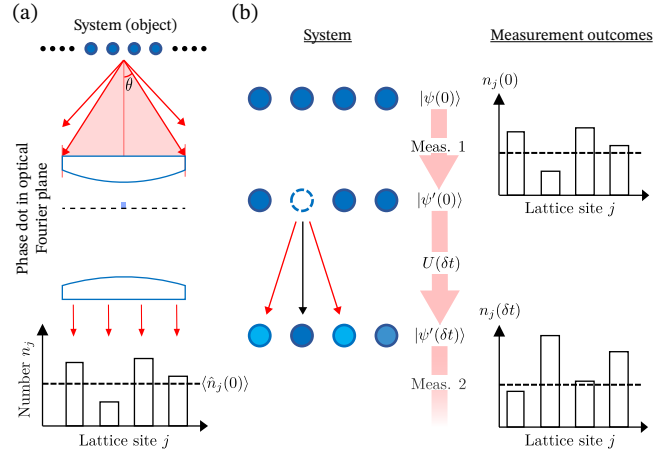


FIG. 1. System and measurement schema. (a) Homodyne detection implemented via PCI. Probe light is first phase shifted by the atomic ensemble (light scattered by more than the acceptance angle θ is not detected); the un-scattered light is further phase shifted by a phase dot; and the resulting imaged intensity. The detected signal (histogram) has contributions from the operator expectation value (dashed line) as well as projection noise. (b) The first measurement creates excitations that are correlated with the measurement outcome and propagate for a time δt prior to a second measurement.

context, where they will allow the extraction of multi-time correlation functions, valid independent of quantum statistics and dimensionality. We specifically focus on homodyne weak measurement schemes [for example, realized by phase-contrast imaging (PCI) as shown in Fig. 1(a)] of atoms in a 1D lattice that report $n_j(t)$, a noisy estimate of number at lattice site j density, and yield post-measurement wavefunctions that incorporate

density fluctuations inferred from the measurement. The resulting excitations propagate for a time delay δt prior to a second weak measurement of density giving $n_j(\delta t)$, as in Fig. 1(b). Intuitively the second measurement outcome includes a contribution from the system's response to the first measurement, and we analytically confirm that the ensemble average [14] of such observations $n_0(0)n_j(\delta t)$, converges to the real part of the un-equal time correlation function $\text{Re}[\langle \hat{n}_0(0)\hat{n}_j(\delta t) \rangle]$. We numerically study an implementation of this approach for the 1D Bose-Hubbard (BH) model, and show that in the limit of vanishing measurement strength $S(q, \omega)$ obtained by the weak measurement process converges to that directly computed from the underlying wavefunctions. We conclude by showing that this method robustly captures long wavelength excitations even with realistic imaging limitations included.

Homodyne detection— Our weak measurement protocol is based on homodyne detection, which could be experimentally implemented using PCI as schematically depicted in Fig. 1(a). When illuminated with coherent light of wavelength λ , an atomic ensemble in the object plane diffracts part of the probe laser by imprinting a position-dependent phase shift onto it. PCI is usually operated in the far-detuned limit, where absorption can be ignored, so the optical intensity just beyond the atomic ensemble is unchanged. By design, PCI is sensitive to changes in the phase quadrature: a phase dot at the Fourier plane of a Keplerian telescope phase shifts the unscattered light by a known phase value (typically $\pi/2$) [15]. In the image plane, the interference between scattered light and the phase-shifted probe changes the detected intensity by an amount proportional to the atomic density. The usual “photon shot noise” in this image is the projection noise associated with detecting the intensity of a coherent state. For a bright beam, this leads to Gaussian backaction on the atomic density.

Analytical derivation— To be concrete, we consider bosonic atoms in a 1D lattice with native system Hamiltonian \hat{H}_{BH} , describing the BH model, responsible for coherent dynamics. These dynamics are interjected by brief homodyne measurements of the atomic density, with durations short compared to the time scale for coherent evolution. Each measurement, at a discrete time t , gives an outcome

$$n_{j,t} = \langle \hat{n}_j(t) \rangle + \frac{m_{j,t}}{2\Gamma^{1/2}}, \quad (1)$$

where Γ is the measurement strength; \hat{n}_j is the number operator at position j ; and $\langle \hat{n}_j(t) \rangle \equiv \langle \psi(t) | \hat{n}_j | \psi(t) \rangle$ is the Schrödinger picture expectation value of number. The random variable $m_{j,t}$, with variance $\overline{m_{j_1,t_1}m_{j_2,t_2}} = \delta_{j_1,j_2}\delta_{t_1,t_2}$, describes spatially and temporally uncorrelated quantum projection noise. For small Γ , the state

conditioned on this measurement outcome [16] is

$$|\psi'(t)\rangle = \left(1 + \Gamma^{1/2} \sum_j \delta\hat{n}_{j,t} m_{j,t} - \frac{\Gamma}{2} \sum_j \delta\hat{n}_{j,t}^2\right) |\psi(t)\rangle \quad (2)$$

in terms of the difference operator $\delta\hat{n}_{j,t} \equiv \hat{n}_j - \langle \hat{n}_j(t) \rangle$.

In our protocol [illustrated in Fig. 1(b)], we (1) perform an initial measurement at time $t = 0$; (2) allow the system to undergo unitary evolution described by $\hat{U}(\delta t) = \exp(-i\hat{H}_{\text{BH}}\delta t/\hbar)$ for a time δt ; and (3) perform a second measurement. We focus on the cross-correlation of the measurement results

$$\overline{n_{j,0}n_{j',\delta t}} = \frac{1}{2\Gamma^{1/2}} \overline{m_{j,0}\langle \hat{n}_{j'}(\delta t) \rangle'} + \overline{\langle \hat{n}_j(0) \rangle \langle \hat{n}_{j'}(\delta t) \rangle'}. \quad (3)$$

Terms such as $\overline{m_{j',\delta t}\langle \hat{n}_{j,0} \rangle}$ are absent in this expression because the number at earlier times is uncorrelated with measurement noise at later times. By contrast, $\langle \hat{n}_{j',\delta t} \rangle$ can be correlated with the noise $m_{j,0}$. We adopt a notation where expectation values with a prime

$$\langle \hat{n}_{j'}(\delta t) \rangle' = \langle \psi'(0) | \hat{U}^\dagger(\delta t) \hat{n}_{j'} \hat{U}(\delta t) | \psi'(0) \rangle \quad (4)$$

are with respect to the post measurement initial state. To lowest order, the expectation value of the number at time δt is

$$\begin{aligned} \langle \hat{n}_{j'}(\delta t) \rangle' &= \langle \hat{n}_{j'}(\delta t) \rangle + \Gamma^{1/2} \sum_j m_{j,0} \left[\langle \hat{n}_j(0) \hat{n}_{j'}(\delta t) \rangle \right. \\ &\quad \left. + \langle \hat{n}_{j'}(\delta t) \hat{n}_j(0) \rangle - 2\langle \hat{n}_j(0) \rangle \langle \hat{n}_{j'}(\delta t) \rangle \right]. \end{aligned}$$

Substituting this expression into Eq. (3) yields $\overline{n_{j,0}n_{j',\delta t}} = \text{Re}[\langle \hat{n}_j(0)\hat{n}_{j'}(\delta t) \rangle]$, equal to the expectation value of the Hermitian part of $\hat{n}_j(0)\hat{n}_{j'}(\delta t)$. This gives direct access to the spatially averaged correlation function

$$G_{\delta j}(\delta t) = \frac{1}{N} \sum_j \text{Re}[\langle \hat{n}_j(0)\hat{n}_{j+\delta j}(\delta t) \rangle], \quad (5)$$

as a function of spatial displacement δj , known as the Van Hove function [17] in x-ray and neutron scattering. This demonstrates our central observation: for $\Gamma \ll 1$, correlating subsequent measurement results yields time-separated correlation functions. This is a generic observation valid for pairwise combinations of weak measurements (potentially of different observables) with the general structure in Eqs. (1)-(2).

The DSF

$$S(q, \omega) = \sum_{\delta j} \int_0^\infty G_{\delta j}(\delta t) e^{i(\omega\delta t - q\delta j)} d\delta t \quad (6)$$

is the Fourier transform of the correlation function. In the subsequent sections, we present concrete numerical

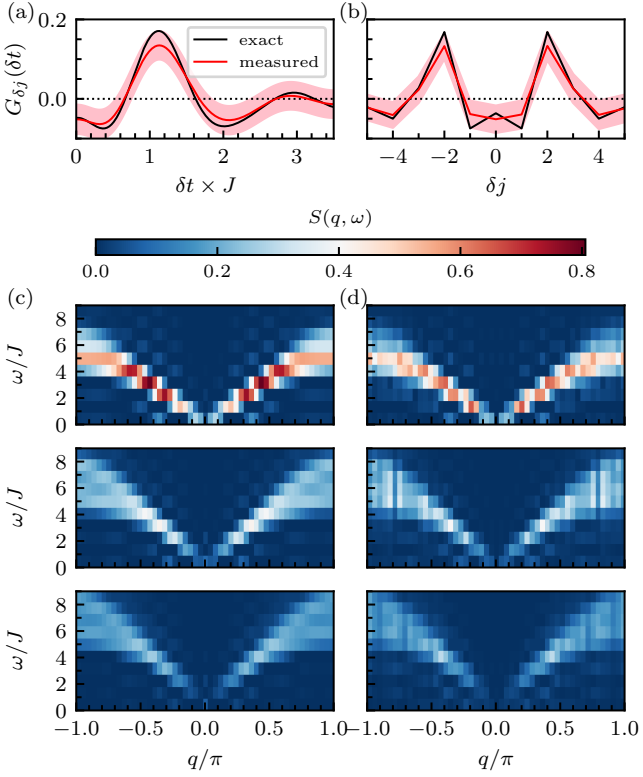


FIG. 2. Averaged correlation function and DSF of a 51-site 1D BH chain with measurement strength $\Gamma = 0.1$, 50 trajectories, and the noise contribution removed from the second measurement. Statistical uncertainties and spatial resolution limits are detailed in the text and presented in Figs. 3 and 4 respectively. (a,b) Correlation signal with $U/J = 2$ at: (a) fixed $\delta j = 2$, and (b) at fixed $\delta t \times J = 1.17$. The black curves were computed directly from MPS wavefunctions, while the red curves employed Eq. (5) (red bands reflect the single- σ uncertainties derived from our 50 trajectories). (c, d) DSF computed for $U/J = 2, 4$, and 5 (top to bottom); (c) DSF from MPS wavefunctions, and (d) DSF obtained from Eq. (6).

examples as to how accurately this quantity can be captured with a realistic measurement strength.

Weakly measured BH system—We now turn to the BH model with Hamiltonian

$$\hat{H}_{\text{BH}} = -J \sum_j \left(\hat{a}_j^\dagger \hat{a}_{j+1} + \text{H.c.} \right) + \frac{U}{2} \sum_j \hat{n}_j (\hat{n}_j + 1),$$

where \hat{a}_j^\dagger describes the creation of a boson on site j and $\hat{n}_j = \hat{a}_j^\dagger \hat{a}_j$ is the associated number operator. We limit the numerical study to 1D and simulate the dynamics using the time-dependent variational principle applied to matrix product states (MPS) [18].

We numerically obtain the ground state $|\psi(0)\rangle$, and then initiate a specific trajectory by stochastically selecting a realization of the projection noise $m_{j,t=0}$. This allows us to compute the associated post-measurement state $|\psi'(0)\rangle$ using Eq. (2) and measurement outcome $n_{j,0}$. The next step is to evolve the resulting state according to \hat{H}_{BH} for a time δt , obtain $\langle \hat{n}_j(\delta t) \rangle$, select a

second noise realization $m_{j,\delta t}$, and thereby obtain the second measurement outcome $n_{j,\delta t}$. We then average the correlation signal [Eq. (3)] over trajectories. To increase sampling efficiency in the numerical simulations, we use each initial noise realization $m_{j,t=0}$ to generate the full collection of second measurement outcomes, by computing $\langle \hat{n}_j(\delta t) \rangle$ and $m_{j,\delta t}$ at every desired measurement time. When reporting correlation functions, we further enhance the sampling efficiency by omitting the noise contribution to the second measurement, giving $n_{j,\delta t} = \langle \hat{n}_j(\delta t) \rangle$. The number of trajectories quoted in the figure captions reflects the number of distinct initial noise realizations.

Figure 2 plots the results of these simulations (see caption for simulation parameters); (a) and (b) show δt and δj cross-sections of the correlation function $G_{\delta j}(\delta t)$ with quantities extracted directly from MPS wavefunctions (black), and those obtained using Eq. (5) (red) agreeing within the statistical uncertainty (error bands). The duration of the MPS simulations are limited to the short times— $\delta t \times J \lesssim 3$ for current parameters—for which they are numerically exact (i.e., converged in truncation error per-timestep); this blocks numerical access to small ω when computing $S(q, \omega)$. Longer times (and therefore smaller ω) are experimentally accessible, however, finite size effects will appear for large δt .

Panels (c) and (d) confirm that $S(q, \omega)$ extracted from the MPS wavefunction (left) is in correspondence with that obtained from the correlation signal (right). The key features of the excitation spectrum [19] are present: in the superfluid phase ($U/J = 2$) a gapless phonon mode (linear for small ω) is present; and in the Mott insulating phase ($U/J = 4, 5$) a energy gap clearly appears. In both cases the DSF contains sharp spectra features derived from well defined quasiparticle excitations: phonons in the superfluid phase giving way to particle-like excitations in the Mott phase.

Systematic and statistical uncertainties—Any determination of $S(q, \omega)$ will have statistical uncertainties resulting from employing only a finite number of trajectories given the noise inherent in the measurement process. In addition, our expressions for spatial correlations and the DSF are only strictly valid when $\Gamma \rightarrow 0$, giving corrections to Eq. (3) at order $\Gamma^{1/2}$, i.e., systematic uncertainties. Both measurements [Eq. (1)] have statistically independent noise contributions $\propto \Gamma^{-1/2}$. (While noise on the second measurement can be neglected when computing averaged quantities, it must be included when computing uncertainties.) Together these contribute a $\propto \Gamma^{-1}$ statistical uncertainty to the correlation function $G_{\delta j}(\delta t)$. In the strong-measurement limit the noise contribution of the second measurement can be neglected, and the remaining statistical uncertainty becomes independent of Γ .

Figure 3(a) and (b) quantify the statistical and total uncertainties at small and large Γ respectively. The green curves plot the standard error of the mean across

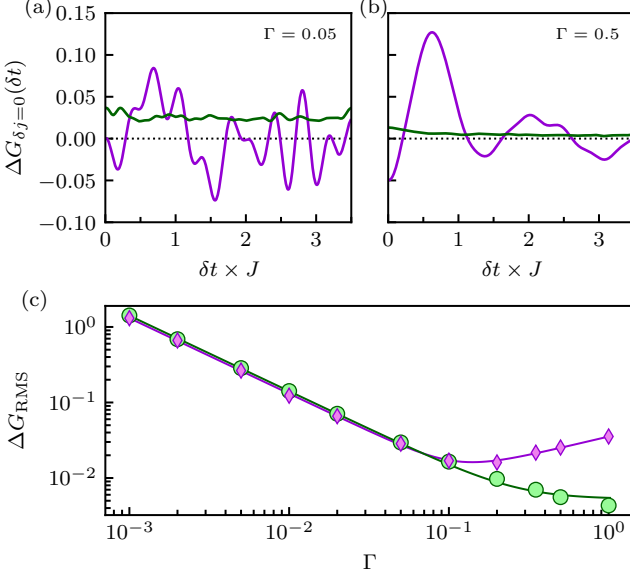


FIG. 3. Statistical and systematic uncertainties using 50 trajectories and $U/J = 2$. (a,b) Comparison of statistical uncertainty (green) and total error (purple) in $\Delta G_{\delta j=0}(\delta t)$ for $\Gamma = 0.05$ and $\Gamma = 0.5$. (c) Statistical (green) and total (purple) uncertainties averaged over δt and δj along with fits (curves) to the scaling behavior described in the text. The statistical uncertainties associated with these averages are smaller than the plotted markers.

50 trajectories (i.e., statistical uncertainty), and the purple curves plot the difference between $G_{\delta j}(\delta t)$ determined exactly from MPS wavefunctions and from our weak measurement approach (with contributions from both statistical and systematic sources). At small Γ , statistical uncertainties exceed systematic effects, making the total and statistical uncertainties comparable; for large Γ the relative importance reverses, so the total uncertainty exceeds the statistical contribution. This is summarized in (c) which plots the overall uncertainties ΔG_{RMS} , the quadratic mean averaged across all δt and the spatial range $\delta j = -10$ to 10, where there is significant signal. As expected, the statistical uncertainty (green) initially decreases as Γ^{-1} before beginning to saturate at large Γ . As suggested by (a) and (b), the combined uncertainty (purple) is dominated by statistical effects for small Γ and systematic effects for large Γ , where it scales as $\propto \Gamma^{1/2}$. The solid curves in Fig. 3(c) confirm these observations with fits to the quadratic mean of the asymptotic scaling behaviors: $[(A\Gamma^{-1})^2 + B^2]^{1/2}$ and $[(A\Gamma^{-1})^2 + (C\Gamma^{1/2})^2]^{1/2}$ for statistical and total uncertainties respectively (with fit parameters A , B , and C). In practice an optimal measurement strategy balances these two sources of uncertainty; in our 50-trajectory simulations these contributions are comparable at $\Gamma = 0.1$.

Resolution limits— Even aside from technical considerations associated with imperfect imaging system design, realistic imaging systems only capture light scattered at

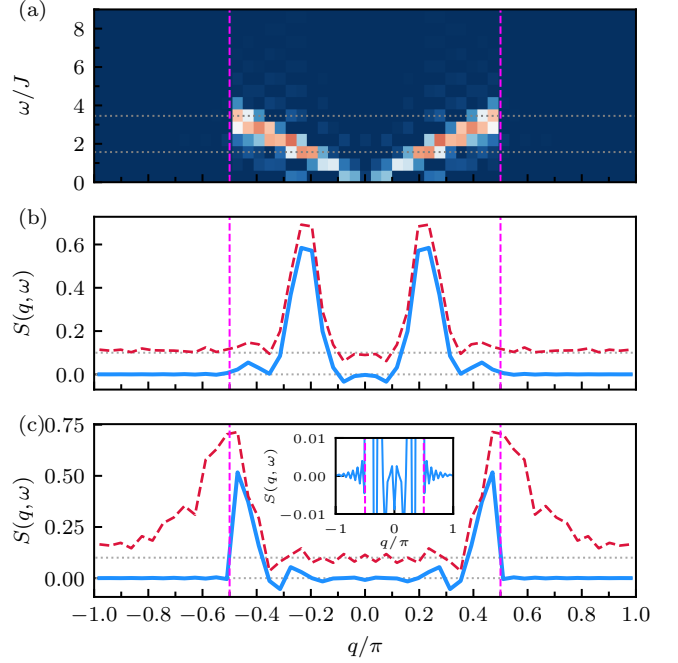


FIG. 4. DSF derived from measurements with imaging resolution effects ($k_{\text{max}} = 0.5$, vertical dashed lines) computed for $U/J = 2$. As in Fig. 2, the noise contribution is removed from the second measurement. The resolution-limited DSF is plotted in (a) using the same color scale as in Fig. 2, while (b) and (c) show cross sections taken at $\omega/J = 1.57$ and $\omega/J = 3.46$ and with (blue) and without (red, offset for clarity) resolution limits. The inset in (c) is vertically expanded to show artifacts outside k_{max} .

angles below an angular acceptance θ ; this introduces a momentum-space cutoff $k_{\text{max}} = 2\pi \sin \theta / \lambda$ [20]. As a result, far-field imaging such as PCI provides no information for wavenumbers above k_{max} , and for this reason the current generation of PCI experiments cannot perfectly resolve individual lattice sites.

Given the inevitability of such resolution limits, we numerically simulated the impact of finite resolution by applying Fourier cutoffs (removing all Fourier components beyond some k_{max}) to the measurement outcomes $n_{j,t}$ prior to computing correlation functions. Figure 4(a) shows the DSF obtained in this way is largely unchanged for $|k| < k_{\text{max}}$ (vertical magenta dashed lines) but is abruptly cutoff at k_{max} . Panels (b) and (c) continue by plotting cross sections taken at $\omega/J = 1.57$ and $\omega/J = 3.46$ [horizontal dashed lines in (a)] both with (blue) and without (red) this cutoff. In (b) the sharp spectral feature is clearly resolved and the DSF is essentially unchanged for $|k| < k_{\text{max}}$. In (c) the cutoff intersects the spectral feature and additional deviations appear: for smaller k the DSF differs from the no-cutoff case, and the $|k| > k_{\text{max}}$ signal (inset) oscillates around zero. Taken together these data confirm that experimentally realistic imaging systems can obtain the DSF associated with long-wavelength excitations up to their k_{max} ,

with worse-case artifacts at the $\approx 5\%$ level.

Conclusion and outlook—Here, we described an experimentally realistic technique employing a pair of weak measurements to extract $S(q, \omega)$, a four-field correlation function; although our study focused on degenerate Bose gases, this method is equally applicable to Fermi gases, Bose-Fermi mixtures, and spin systems. Other techniques for measuring $S(q, \omega)$, such as Bragg spectroscopy, detect the system’s response to experimentally induced perturbations. Therefore, separate technical infrastructure is required to create excitations at each desired q and ω , and then to measure the response. From this practical perspective, our method reduces experimental complexity as it relies on measurements alone. We note that systems described by non-Hermitian evolution can also provide access to correlation functions of this type [21, 22].

As briefly noted above, this approach can be used to obtain more exotic two-time correlation functions of any pair of Hermitian operators that can be weakly measured. Such a process yields the expectation value of the $O(\Gamma^{1/2})$ backaction operator of the first measurement [e.g., $\delta\hat{n}_j$ in Eq. (2)] multiplied by the measurement operator of the second measurement [e.g., $\hat{n}_{j'}$ in Eq. (4)]. Examples include spin-spin correlation functions such as $\langle \hat{n}_{j,\uparrow} \hat{n}_{j',\downarrow} \rangle$ in multi-component (or even multi-species) systems and even hybrid spatial-momentum correlations $\langle \hat{n}_j \hat{n}_k \rangle$ that combine the momentum space number density \hat{n}_k with the real space density.

A straightforward extension of this scheme to three measurements provides access to a weak-measurement Leggett-Garg [23, 24] correlation function $B_{j_1, j_2} = \overline{n_{j_1, t_1} n_{j_2, t_2}} + \overline{n_{j_1, t_2} n_{j_2, t_3}} - \overline{n_{j_1, t_1} n_{j_2, t_3}}$. Leggett-Garg correlation functions obey Bells inequality-like relations that distinguish between classical and quantum correlations. Here violations of a Leggett-Garg inequality may identify non-trivial entanglement in self-equilibrating closed systems, even when the eigenstate thermalization hypothesis is otherwise valid for local degrees of freedom [25].

Extensions of this approach that directly correlate more than two measurements access higher order correlation functions, however, the resulting signal derives from higher order moments of the random variable $m_{j,t}$ and are dwarfed by two-point correlators (with sufficient statistics higher same-time correlations have been observed [26]). It is possible, therefore, that such extensions may even yield out of time ordered correlations with their ability to quantify quantum chaos and entanglement spreading [27].

The authors thank J. K. Thompson for productive discussions, D. Barker and L. P. Garcia-Pintos for carefully reading the manuscript. Additionally, L. P. Garcia-Pintos identified the connection to Leggett-Garg inequalities. This work was partially supported by the National Institute of Standards and Technology; the National Science Foundation through the Quantum Leap Challenge Institute for Robust Quantum Simulation (grant OMA-

2120757); and the Air Force Office of Scientific Research Multidisciplinary University Research Initiative “RAP-SYDY in Q” (FA9550-22-1-0339).

- [1] N. W. Ashcroft and N. D. Mermin, *Solid State Physics* (Harcourt Brace College Publishers, 1976).
- [2] K. Sturm, *Zeitschrift für Naturforschung A* **48**, 233 (1993).
- [3] J. Steinhauer, R. Ozeri, N. Katz, and N. Davidson, *Phys. Rev. Lett.* **88**, 120407 (2002).
- [4] J. M. Pino, R. J. Wild, P. Makotyn, D. S. Jin, and E. A. Cornell, *Phys. Rev. A* **83**, 033615 (2011).
- [5] R. Landig, F. Brennecke, R. Mottl, T. Donner, and T. Esslinger, *Nature Communications* **6**, 7046 (2015).
- [6] H. Biss, L. Sobirey, N. Luick, M. Bohlen, J. J. Kinnunen, G. M. Bruun, T. Lompe, and H. Moritz, *Phys. Rev. Lett.* **128**, 100401 (2022).
- [7] P. T. Brown, E. Guardado-Sánchez, B. M. Spar, E. W. Huang, T. P. Devereaux, and W. S. Bakr, *Nature Physics* **16**, 26 (2020).
- [8] A. Bohrdt, E. Demler, F. Pollmann, M. Knap, and F. Grusdt, *Phys. Rev. B* **102**, 035139 (2020).
- [9] A. Bohrdt, E. Demler, and F. Grusdt, *Phys. Rev. Lett.* **127**, 197004 (2021).
- [10] C.-L. Hung, X. Zhang, L.-C. Ha, S.-K. Tung, N. Gemelke, and C. Chin, *New Journal of Physics* **13**, 75019 (2011).
- [11] C. Guerlin, J. Bernu, S. Deléglise, C. Sayrin, S. Gleyzes, S. Kuhr, M. Brune, J.-M. Raimond, and S. Haroche, *Nature* **448**, 889 (2007).
- [12] Z. K. Minev, S. O. Mundhada, S. Shankar, P. Reinhold, R. Gutiérrez-Jáuregui, R. J. Schoelkopf, M. Mirrahimi, H. J. Carmichael, and M. H. Devoret, *Nature* **570**, 200 (2019).
- [13] H. M. Wiseman and G. J. Milburn, *Quantum Measurement and Control* (Cambridge University Press, 2009).
- [14] The ensemble can include trajectories for a single initial pure state, or different initial states sampled from a specified distribution.
- [15] E. Altuntas and I. B. Spielman, *Phys. Rev. Research* **3**, 043087 (2021).
- [16] M. B. Plenio and P. L. Knight, *Rev. Mod. Phys.* **70**, 101 (1998).
- [17] L. Van Hove, *Phys. Rev.* **95**, 249 (1954).
- [18] J. C. Bridgeman and C. T. Chubb, *Journal of Physics A: Mathematical and Theoretical* **50**, 223001 (2017).
- [19] M. P. A. Fisher, P. B. Weichman, G. Grinstein, and D. S. Fisher, *Physical Review B* **40**, 546 (1989).
- [20] In addition, for systems that are spatially extended along the imaging axis by more than the depth of field, the whole system cannot be simultaneously in focus; this leads to an effective reduction in the NA. Here our focus is on very strong transverse confinement, making this second effect negligible.
- [21] A. Schuckert and M. Knap, *Phys. Rev. Res.* **2**, 043315 (2020).
- [22] L. Pan, X. Chen, Y. Chen, and H. Zhai, *Nature Physics* **16**, 767 (2020).
- [23] A. J. Leggett and A. Garg, *Phys. Rev. Lett.* **54**, 857 (1985).
- [24] A. N. Jordan, A. N. Korotkov, and M. Büttiker, *Phys.*

Rev. Lett. **97**, 026805 (2006).

[25] M. Rigol, V. Dunjko, and M. Olshanii, Nature **452**, 854 (2008).

[26] T. Schweigler, V. Kasper, S. Erne, I. Mazets, B. Rauer, F. Cataldini, T. Langen, T. Gasenzer, J. Berges, and J. Schmiedmayer, Nature **545**, 323 EP (2017).

[27] E. B. Rozenbaum, S. Ganeshan, and V. Galitski, Phys. Rev. Lett. **118**, 086801 (2017).